Journal of Applied Physics

Ferroelectrics everywhere: Ferroelectricity in magnesium substituted zinc oxide thin films

Cite as: J. Appl. Phys. **130**, 044101 (2021); https://doi.org/10.1063/5.0053755
Submitted: 10 April 2021 . Accepted: 03 July 2021 . Published Online: 22 July 2021

Kevin Ferri, Saiphaneendra Bachu, Wanlin Zhu, Mario Imperatore, John Hayden, Nasim Alem, Noel Giebink, Susan Trolier-McKinstry, and Jon-Paul Maria

Journal of Applied Physics ARTICLE scitation.org/journal/jap

Ferroelectrics everywhere: Ferroelectricity in magnesium substituted zinc oxide thin films

Cite as: J. Appl. Phys. **130**, 044101 (2021); doi: 10.1063/5.0053755
Submitted: 10 April 2021 · Accepted: 3 July 2021 ·
Published Online: 22 July 2021

View Online Export Citation CrossMark

Kevin Ferri,[1,a)] Saiphaneendra Bachu,[1] Wanlin Zhu,[1] Mario Imperatore,[2] John Hayden,[1] Nasim Alem,[1] Noel Giebink,[2] Susan Trolier-McKinstry,[1] and Jon-Paul Maria[1]

AFFILIATIONS

[1]Department of Materials Science and Engineering, The Pennsylvania State University, University Park, Pennsylvania 16801, USA
[2]Department of Electrical and Computer Engineering, The Pennsylvania State University, University Park, Pennsylvania 16801, USA

[a)]**Author to whom correspondence should be addressed:** kzf84@psu.edu

ABSTRACT

We demonstrate ferroelectricity in Mg-substituted ZnO thin films with the wurtzite structure. $Zn_{1-x}Mg_xO$ films are grown by dual-cathode reactive magnetron sputtering on (111)-Pt // (0001)-Al_2O_3 substrates at temperatures ranging from 26 to 200 °C for compositions spanning from x = 0 to x = 0.37. X-ray diffraction indicates a decrease in the *c*-lattice parameter and an increase in the *a*-lattice parameter with increasing Mg content, resulting in a nearly constant *c*/*a* axial ratio of 1.595 over this composition range. Transmission electron microscopy studies show abrupt interfaces between $Zn_{1-x}Mg_xO$ films and the Pt electrode. When prepared at $pO_2 = 0.025$, film surfaces are populated by abnormally oriented grains as measured by atomic force microscopy for Mg concentrations >29%. Raising pO_2 to 0.25 eliminates the misoriented grains. Optical measurements show increasing bandgap values with increasing Mg content. When prepared on a 200 °C substrate, films display ferroelectric switching with remanent polarizations exceeding 100 $\mu C\,cm^{-2}$ and coercive fields below 3 MV cm^{-1} when the Mg content is between ~30% and ~37%. Substrate temperature can be lowered to ambient conditions, and when doing so, capacitor stacks show only minor sacrifices to crystal orientation and nearly identical remanent polarization values; however, coercive fields drop below 2 MV/cm. Using ambient temperature deposition, we demonstrate ferroelectric capacitor stacks integrated directly with polymer substrate surfaces.

INTRODUCTION

Polarization reversal is a distinguishing feature in ferroelectric crystals from which functionalities like nonvolatile information storage and surface charge modulation emerge. Integrating these properties with mainstream semiconductors has been achieved, but the transformative impact that was originally conceived remains elusive.[1–3] Regarding conventional perovskite ferroelectrics, incompatible windows for synthesis and difficulties with scaling to dimensions below ~100 *nm* are chief among factors prohibiting integration[4,5] Currently, it appears that harnessing the full capabilities of highly scaled, integrated ferroelectrics requires a different material set, perhaps beyond the perovskite titanate palette that historically inspired the electroceramics field.[6–8]

To find such new materials, it is worth considering structurally simpler polar crystals and exploring the possibility that some combination of preparation and formulation may render their polar axes re-orientable. Hints toward this concept are present in the literature, for example, in 1952 by von Hippel,[9] in 1957 by Megaw,[10] and in 1985 by Burns;[11] however, broad studies that test this concept have not been reported. Two novel ferroelectric materials were developed in the past decade that invite a focused investigation: HfO_2 and $Al_{1-x}Sc_xN$.[12,13] In HfO_2, factors including strain, grain size, and defect chemistry can stabilize a switchable polar phase, while in AlN, substituting ~20% Sc for Al (and more recently ~2% B[14]) will accomplish the same. These reports direct our community to a rich new composition horizon, where every polar crystal is a possible ferroelectric host with the correct persuasion. The myriad possibilities demand a structured approach, and ours rests on the tenet that structural distortions emerge in polar solid solution crystals at compositions approaching a transition to the phase-separated state. Such formulations are purposefully poised in proximity to a structural instability, where one anticipates a softened structural energy landscape with an increased chance for

polarization reversal. Essentially, we extend the concept of enhanced piezoelectric coefficients in AlN and ZnO by dissolving a misfit cation into a polar structure to enable field-induced reorientation—in doing so, we may find ferroelectricity everywhere.

Tantalizing examples are available to guide our study; consider the Ta_2O_5–TiO_2 system for which Cava *et al.* in 1995 and Brennecka and Payne in 2006 showed enhanced permittivity values up to 260 for ∼8% Ti substitution.[15,16] This value is too large for the ionic and electronic polarizabilities of the associated ions as predicted by Shannon and Prewitt,[52] so additional mechanisms must also contribute. It is worth noting that 8% Ti is close to the solubility boundary neighboring the first two-phase field in the Ta_2O_5–TiO_2 phase diagram. As the composition approaches this boundary, stronger distortions and a larger structural polarizability may promote polarity and the possibility for a strong nonlinear response. These ideas are speculative but worth considering in the search for new ferroelectric systems. This paper explores the connection between chemical stress/disorder and polarization reversal as a general phenomenon in the ZnO–MgO system. In doing so, we expand our understanding of an isomorphous oxide system compared to that explored by Fichtner *et al.*[13] and Hayden *et al.*[14] to make an initial test of a "ferroelectrics everywhere" hypothesis.

ZnO is a II-VI wurtzite semiconductor with a 3.4 eV bandgap and $\sim 90\,\mu C\,cm^{-2}$ spontaneous polarization along the [0001] direction.[17] ZnO is regarded conventionally as non-ferroelectric. However, as demonstrated in AlN, polarization reversal may be triggered if the appropriate chemical "stressors" are applied. Unlike AlN, the ZnO bandgap is only 3.4 eV; thus, an appropriate substituent must boost the bandgap if the coercive fields are also large. In this case, the ideal stressor is Mg, since its binary oxide has a bandgap of 7.8 eV, and many authors have shown that more than 40 mol. % can be stabilized in a wurtzite solid solution.[18–22] Onodera *et al.* reported ferroelectricity in the $Zn_{1-x}(Mg,Li)_xO$ system, but polarization values are small ($0.06–0.9\,\mu C\,cm^{-2}$) and room temperature loss tangents are large (∼0.5).[23–27] In 2003, Emanetoglu *et al.* proposed this system as a means to tailor acoustic velocities and piezoelectric coupling coefficients for optimized acoustic wave devices.[28] In parallel, the ZnO–MgO ($Zn_{1-x}Mg_xO$) system was broadly investigated by the wide bandgap semiconductor[20,22,29,30] and photovoltaic communities,[31,32] as an optoelectronic solid solution whose bandgap could be tuned between 3.3 and 4.5 eV. Similarly, Kang *et al.* demonstrated that ZnO thin films substituted with 35% MgO show a 360% and 290% increase to the out-of-plane ($d_{33,f}$) and in-plane ($e_{31,f}$) piezoelectric coefficients, respectively,[19] as was shown by many authors in the $Al_{1-x}Sc_xN$ system.[33,34] Given the structural and piezoelectric similarities between $Al_{1-x}Sc_xN$ and $Zn_{1-x}Mg_xO$, we explore the possibility of ferroelectric switching in this wurtzite solid solution.

EXPERIMENTAL PROCEDURE

Ferroelectric $Zn_{1-x}Mg_xO$ thin films were prepared by radio frequency (RF) magnetron co-sputtering from 1-in. Zn and Mg (99.9999% and 99.95% purity, respectively) metallic targets held at a 3 cm target-to-substrate working distance. Substrates consisted of $1 \times 1\,cm^2$ single crystal (0001)-Al_2O_3 pieces cleaved from 4 in. diameter wafers. Prior to deposition, substrates were prepared by rinsing in a solvent (isopropanol and methanol) for 30 s, followed by a 10-min ultraviolet–ozone treatment, before being heated to 300 °C and pumped to a 1.0×10^{-7} Torr base pressure. Highly oriented 100 nm thick (111)-Pt films were deposited as blanket bottom electrodes via direct-current (DC) magnetron sputtering from a metallic Pt (99.99% pure) target held at a 6 cm target-to-substrate working distance, before lowering the temperature to 200 °C. Next, 500-nm thick $Zn_{1-x}Mg_xO$ films were sputtered at 2.5 mTorr total pressure in a mixed argon–oxygen atmosphere achieved by 20 sccm Ar and 2.5 and 5 sccm O_2 flow rates. To control the Mg concentration, the Zn target voltage (and thus flux) was fixed at 260 V, while the Mg target power was varied between 0 and 60 W. For electrical characterization, 100 nm Ir top electrodes were deposited by a shadow mask using room temperature DC magnetron sputtering. Electrode areas were measured by optical microscopy to ensure an accurate area for permittivity and polarization calculations.

Crystallographic phase, structure, and texturing were characterized using a Panalytical Empyrean x-ray diffractometer. Surface morphology and roughness were studied by an Asylum MFP3D atomic force microscope in the repulsive tapping mode. Internal microstructure was investigated using a Thermo Fisher Talos F200X scanning/transmission electron microscope (S/TEM). An amorphous carbon layer was deposited during the focused ion beam (FIB) sample preparation step to prevent sample damage. Mg:Zn ratios were measured via energy dispersive spectroscopy (EDS) in a Zeiss Sigma scanning electron microscope. Optical measurements were carried out using an Agilent Cary 700 UV-Vis-NIR spectrometer with photon energies ranging from 1.13 to 6.52 eV at a 6° incident angle. Polarization–electric field (P–E) measurements were performed using a Summit 11000B analyzer with a triangular signal at 100 Hz.

RESULTS AND DISCUSSION

First, 500 nm thick $Zn_{1-x}Mg_xO$ films with increasing Mg:Zn ratio were prepared on Pt bottom electrodes and structurally characterized by x-ray diffraction (XRD) using Cu–Kα_1 (1.5406 Å) radiation to determine their crystalline orientation, lattice parameters, and mosaicity. Results for a Mg composition series spanning from 0% to 100% Mg, shown in Fig. 1, reveal the wurtzite crystal structure for 0%–37% Mg and uniform (0001) texturing. For higher Mg concentrations, an additional x-ray peak consistent with {111}-rock salt emerges, suggesting the metastable solubility limit for these conditions. Rocking curves of the 0002 $Zn_{1-x}Mg_xO$ reflection were collected, and full-width-half-max values are given in Fig. 1 next to their respective θ–2θ traces.

All fall between 1.5° and 2.5° and follow a similar trend to films deposited on (111)-Pt substrates.[19] Additionally, (0004) and ($10\bar{1}5$) reflections were scanned and used to calculate the *c*- and *a*-lattice parameters as shown in Fig. 2. With increasing Mg substitution, the *c*-lattice parameter decreases monotonically while the *a*-lattice parameter generally increases, with perhaps a weak maximum at 23% Mg as shown in Figs. 2(a) and 2(b). Since these

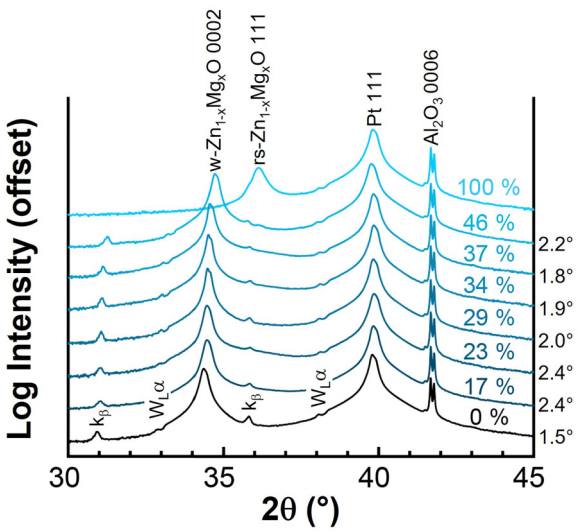

FIG. 1. θ–2θ x-ray diffraction patterns for structural characterization of a $Zn_{1-x}Mg_xO$ composition series ranging from 0% to 100% Mg. Rocking curves of the $Zn_{1-x}Mg_xO$ 0002 reflection are given next to their respective θ-2θ trace.

films are grown at low homologous temperatures and low total pressures (where energetic bombardment can freeze in a highly non-equilibrium local structure), it is important not to over-interpret the lattice constant dependencies. In general, the values of *a* and *c* and their composition dependencies are consistent with the comprehensive report of Jang and Chichibu.[35]

The *c*/*a* ratio for the entire composition series is shown in Fig. 2(c). This ratio is a quantity of interest for wurtzite crystals because it can be related to the crystallographic *u*-parameter, which is an indicator of the structural proximity to the hexagonal, non-polar boron nitride (BN) polymorph. In $Al_{1-x}Sc_xN$, *c*/*a* falls sharply with increasing Sc with an expectation of increasing *u*. For the $Zn_{1-x}Mg_xO$ system, *c*/*a* is ∼1.595 to 1.615 over the entire Mg concentration range and is composition independent in formulations above 17% Mg. Given the strong contrast between *c*/*a* trends in the ZnO–MgO and AlN–ScN systems, at this stage, the general role of such lattice constant trends in promoting/supporting polarization reversal is not clear.

Skew-symmetric azimuthal scans of the Pt (100) and $Zn_{1-x}Mg_xO$ ($10\bar{1}5$) were used to assess the in-plane registry. Two orientations are present for the Pt layer. $Zn_{1-x}Mg_xO$ adopts both of them, producing two orientation domains: $\langle 110\rangle||\langle 0001\rangle$ and $\langle 1\bar{1}0\rangle||\langle 0001\rangle$, that are related by a 30° in-plane rotation. X-ray peaks of the former are 200× more intense than the latter. Phi-scans are provided in the supplemental material (S1) showing these populations.

Microstructure and local orientation relationships were investigated by TEM. Figure 3(a) shows a cross section of $Zn_{1-x}Mg_xO$ (34% Mg), Pt, and Al_2O_3 layers imaged with 200 kV electrons, while Fig. 3(b) is a selected area electron diffraction (SAED) pattern that samples the film, substrate, and bottom electrode layers highlighting their epitaxial registry, i.e., $Zn_{1-x}Mg_xO$ (0001)// Pt (111) // Al_2O_3 (0001). Figures 3(c)–3(h) show the results of STEM-EDS analysis. The most important findings from the analysis are smooth interfaces without strong evidence for chemical mixing (consistent with the low-temperature preparation) and a generally uniform distribution of Zn and Mg. It is important to note that the additional in-plane orientation seen by azimuthal x-ray scans were observed in the TEM cross sections. Detailed SAED analyses are provided in the supplemental material (S1) that confirm the location, size, and distribution of this additional orientation population.

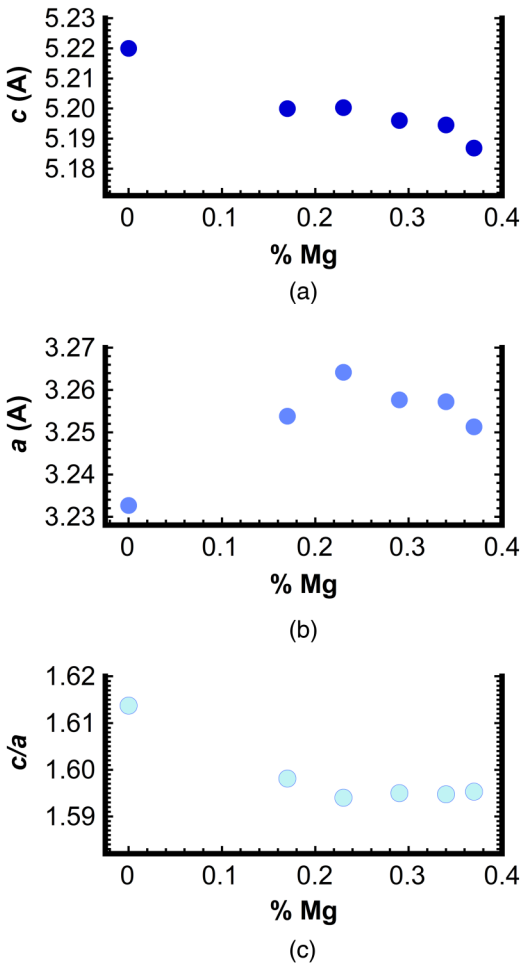

FIG. 2. In-plane (a), out-of-plane (b), and *c*/*a* (c) lattice parameter trends as a function of Mg content.

Atomic force micrographs were collected to determine trends in surface morphology; Fig. 4 shows these results. These measurements indicate decreased grain size with increasing Mg content, which is consistent with the existing $Zn_{1-x}Mg_xO$ literature.[19,36,37] For Mg concentrations greater than 29%, the surfaces are populated by larger faceted grains. Kim *et al.* reported abnormally oriented grain (AOG) growth for $Al_{1-x}Sc_xN$ films deposited by RF-sputtering on Al_2O_3 and a mechanism involving initiation by composition segregation.[37]

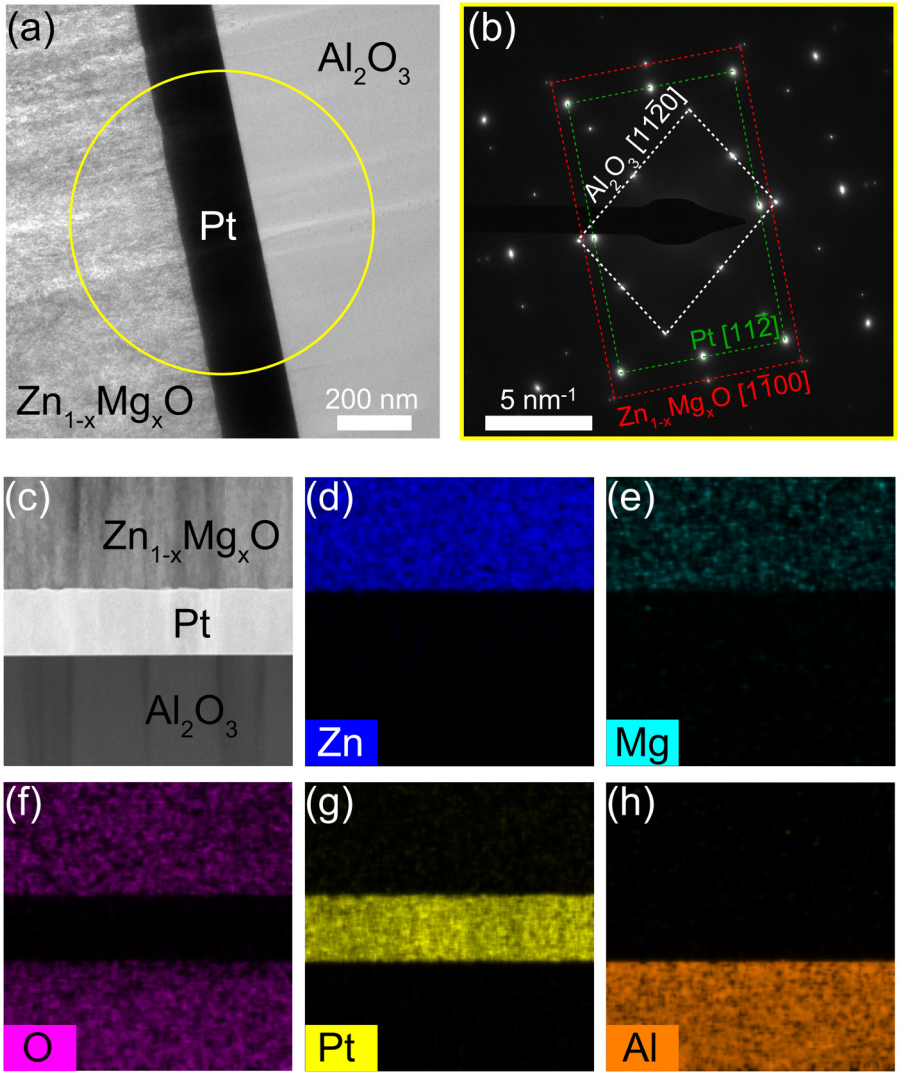

FIG. 3. Transmission electron microscopy (TEM) of a $Zn_{1-x}Mg_xO$ thin film with $x = 0.34$. (a) Bright-field TEM image of the $Zn_{1-x}Mg_xO$ / /Pt // Al_2O_3 layering; (b) selected area electron diffraction pattern from the entire layer stack with underlying epitaxial registry between layers; (c) high angle annular dark field STEM image of the same layer stack; and (d)–(h) STEM-EDS atom percent quantified maps for each constituent element.

Given that AOG formation is observed only at higher concentrations with a formation threshold of ~30% Mg, it is possible that they also result from an onset of chemical segregation that precedes full-phase separation; additional analysis is needed to confirm or refute this relationship.

Unlike the situation for $Al_{1-x}Sc_xN$ where AOGs seem to be difficult to eliminate in ferroelectric compositions, in $Zn_{1-x}Mg_xO$, these microstructural asperities are sensitive to deposition conditions and can be eliminated using several approaches, including temperature and oxygen partial pressure, which may act as additional film stress compensators during growth. As an example, if the oxygen partial pressure is increased from 2.5% O_2 to 25% pO_2, the large surface features are nearly eliminated even at Mg concentrations above 35% as shown in the supplemental material (S2). All subsequent films were prepared under these higher oxygen content conditions. We note that the deposition rate did not change appreciably when transitioning from 2.5% to 25% pO_2, nor did the overall microstructure—besides the lack of AOGs.

It is well known that Mg additions boost the ZnO bandgap to values approaching 4.5 eV.[18,20,38,39] Given an expectation for high coercive fields in ferroelectric ZnO, by analogy to $Al_{1-x}Sc_xN$, it is important to measure this quantity for the present study as these values establish the intrinsic upper limit of breakdown strength. To do so, the composition series was measured by UV-Vis spectrometry in reflection mode; subsequent Tauc fitting was used to determine the optical bandgap. The extracted bandgap for $Zn_{1-x}Mg_xO$ was at 3.2 eV for 0% Mg and steadily rises to a maximum at 4.1 eV for 34% Mg. Tauc fits and bandgap plots are provided in the supplemental material.

Figure 5 shows the low- and high-field dielectric properties for films containing 23%–37% Mg. The hysteresis loops in

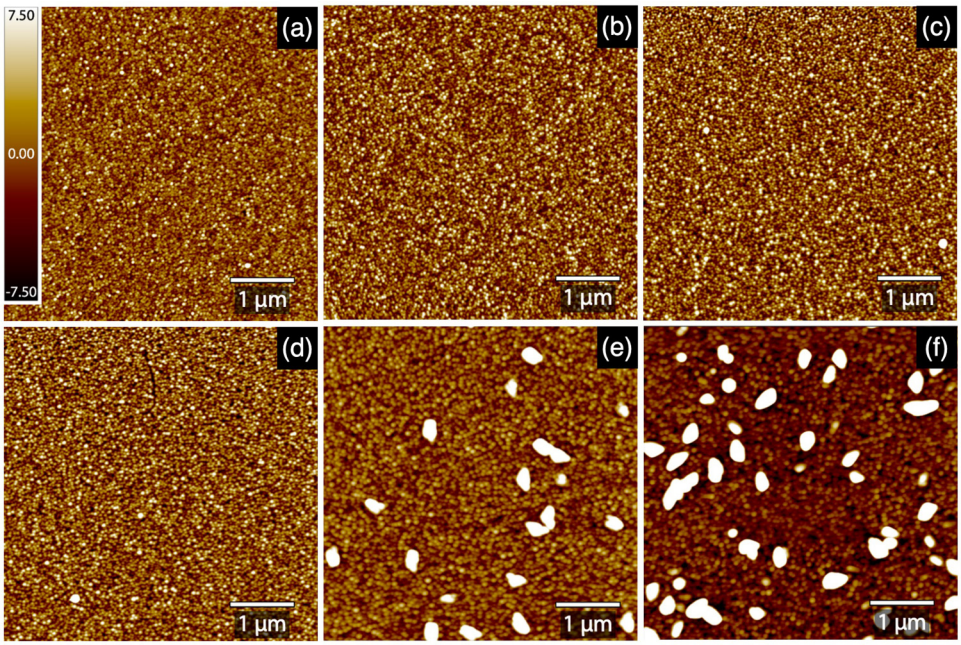

FIG. 4. Atomic force micrographs for $Zn_{1-x}Mg_xO$ thin films ranging in concentration from 0% to 37% Mg [(a)–(f)] incorporation, deposited with an oxygen flow rate of 0.5 sccm. Grains of alternative texture emerge ~34% Mg (c).

Fig. 5(a) show that (1) for 23% and 29% Mg (and all lower values), dielectric breakdown occurs before any indications of non-linear polarization vs field and the electric fields applied in these traces represent the maximum values possible before breakdown; and (2) between 34% and 37% Mg, ferroelectric switching is observed with remanent polarization values above 100 μC cm^{-2} and coercive field values in the vicinity of 2.7 MV cm^{-1}. Figures 5(a) and 5(b) show relative permittivity and loss tangent values for the $Zn_{1-x}Mg_xO$ composition series at 26 °C with a 10 kHz frequency oscillator. In general, loss tangent values decrease with increasing Mg content, which is consistent with the expectation of a larger bandgap. The real part of the permittivity increases with Mg substitutions and reaches a maximum near 40% Mg; more Mg causes phase separation. The increase prior to separation is associated with the ferroelectric phase becoming field-accessible by Mg incorporation and possibly finite dipolar contributions to the permittivity. Low-frequency permittivity values for MgO and ZnO are comparable and well known (~9 and ~10, respectively);[40,41] thus, the changes seen presently are not likely due to changes in ionic or electronic contributions that will occur to a finite degree by chemical substitution.

It is possible that polarization reversal in $Zn_{1-x}Mg_xO$ is facilitated by a point-defect mechanism. While there are some suggestions for this in the literature, the present data set does not support a similar interpretation. Consider that polarization reversal in $Zn_{1-x}Mg_xO$ occurs at Mg > ~30%; if supported by an anion vacancy model, one should anticipate more oxygen non-stoichiometry when adding Mg.

The MgO formation enthalpy is nearly 2× larger than for ZnO (~−600 and ~−350 kJ/mol).[42,43]

As quantified by Lettieri *et al.* in MBE grown Sr-substituted Gd_2O_3, this substitution will produce a more completely oxygenated host crystal under comparable growth conditions than the pure reference, and a lower overall anion defect concentration.[44] Furthermore, the reduction in dielectric loss and ability to survive larger electric fields with increasing Mg incorporation seen presently is more consistent with an overall lower defect concentration. In such a case, there would be a smaller tendency for pseudo-ferroelectric contributions, and thus one does not need to invoke a defect-enabled mechanism for the explanation of ferroelectric switching in the $Zn_{1-x}Mg_xO$ system.

At this state, the authors prefer a cautious approach with minimal speculation regarding the origins of polarization reversal and prefer a general hypothesis where a softened energy landscape accompanies chemical substitution and promotes switching as proposed for $Al_{1-x}Sc_xN$ by Fichtner *et al.*[13] and $Al_{1-x}B_xN$ by Hayden *et al.*[14]

While the hysteresis loops in Fig. 5(a) show stable polarization-field traces that can be reproduced for many cycles, we note that $Zn_{1-x}Mg_xO$ films must undergo a "wake-up" process before repeatable switching. The term "wake-up" is adopted from the perovskite and HfO_2 literature;[45,46] however, at this stage, there is no indication that mechanisms are related. The inset in Fig. 6 illustrates the wake-up process for a 34% Mg film by cycling at 2.8 MV cm^{-1} from 1 to 1000 cycles, and P_r saturates at ~100 cycles.

To illustrate the polarization vs E_{max} relationship, field-dependent P_r measurements were collected on the same capacitor that was first woken up at 2.8 MV cm^{-1} and subsequently exposed to bipolar switching cycles with the increasing maximum electric field. The results are plotted in Fig. 6. They reveal an abrupt

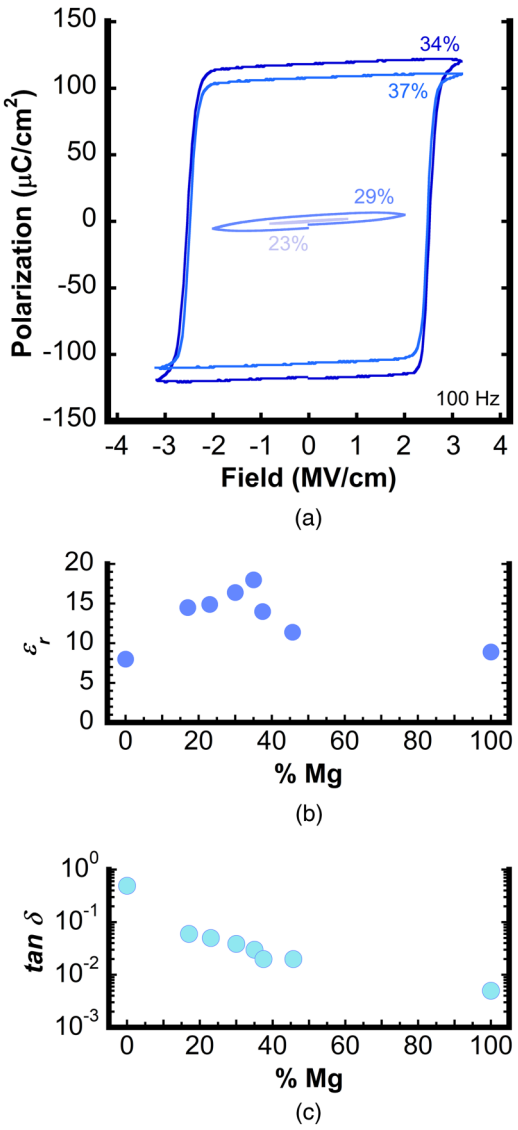

FIG. 5. (a) P–E loops of ferroelectric $Zn_{1-x}Mg_xO$ thin films with Mg contents of x = 0.23, 0.29, 0.34, and 0.37; and low-field real (b) and imaginary (c) dielectric properties of $Zn_{1-x}Mg_xO$ thin films.

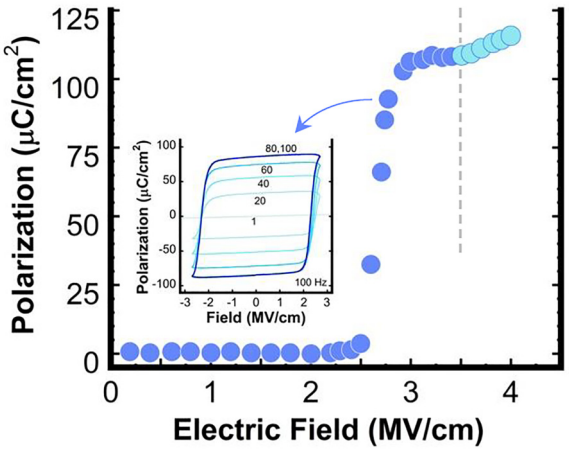

FIG. 6. Remanent polarization vs applied electric field trace for a $Zn_{1-x}Mg_xO$ film with 34% Mg. P_r vs E measurements were used to determine the maximum switchable polarization and saturation region. The transition from dark blue to light blue dots corresponds to the electric field range where leakage current becomes large. The inset provides an example of the wake-up process, and the numbers indicate how many field cycles were applied before the adjacent trace.

increase ~of 2.5 MV cm^{-1} and a polarization plateau of 110 μC^{-2} between 2.8 and 3.5 MV cm^{-1}. Polarization increases with larger electric fields, but this increase can be attributed to leakage contributions. Positive-up-negative-down (PUND) measurements were performed on a fully woken up $Zn_{1-x}Mg_xO$ film with 34% Mg; complete details of the measurement parameters and field-time profiles are given in the supplemental material. The measurement conditions were 100 Hz with four pulses at 2.8 MV cm^{-1} in a 12 ms period. The PUND polarization value is 109 μC cm^{-2}, in close agreement with conventional hysteresis.

All material presented thus far used a substrate manipulator temperature of 200 °C, which translates to a substrate surface temperature (by pyrometry) of ~120 °C. To explore the limits of low-temperature preparation, $Zn_{1-x}Mg_xO$ and Pt layers were deposited without intentional substrate heating. The motivation for this experiment is twofold: (i) while crystallinity may suffer from such low thermal budgets, it is possible that a more favorable defect equilibrium will accompany these conditions; and (ii) room temperature preparation facilitates the simplest possible integration pathways.

Figures 7(a) and 7(b) show x-ray diffraction θ–2θ-scans and polarization hysteresis loops of 34% Mg $Zn_{1-x}Mg_xO$ deposited without intentional substrate heating. Structurally, the material is very similar, but without substrate heating, coercive fields drop by roughly 33% and remanent polarization increases by 20%. While assigning causality is outside the scope of this report and our current understanding, we speculate that quenching to near-room temperature conditions from the vapor phase produces a different defect equilibrium and an easier polarization reversal process. For this experiment, the Pt bottom electrode and the $Zn_{1-x}Mg_xO$ films were fabricated with no substrate heating; however, it is important to note that plasma exposure during the sputtering process increased the substrate puck temperature to 40 °C over the course of a deposition. This increase is expected following the literature that predicts similar behavior for comparable plasma energetics.[47]

While studies thus far utilized exclusively *c*-plane sapphire substrates, this new room temperature deposition capability presents a tantalizing opportunity for ferroelectric capacitors prepared directly on polymer substrates. Polymer-integrated ferroelectric thin films may enable or facilitate applications including smart cards, biomedical sensors, and foldable antennae.[48–51]

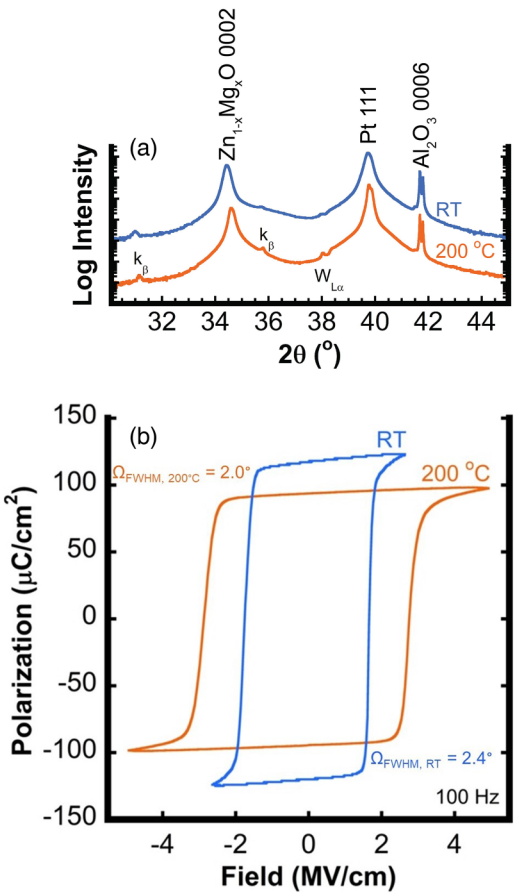

FIG. 7. Comparison of the structural x-ray diffraction θ–2θ scans (a) and electrical polarization hysteresis loops (b) for two $Zn_{1-x}Mg_xO$ films deposited at 200 °C (orange) and 26 °C (blue), respectively. Films deposited at room temperature show nearly identical structural properties.

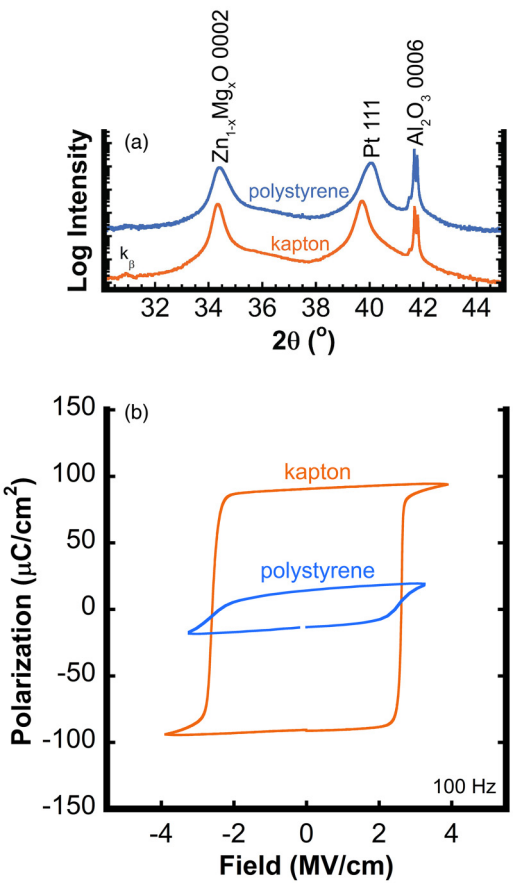

FIG. 8. (a) X-ray diffraction θ–2θ scans, and (b) polarization hysteresis loops collected on Pt|$Zn_{1-x}Mg_xO$ film stacks prepared on polystyrene and Kapton-coated sapphire.

Two polymer substrates were chosen to test this possibility, 150 nm polystyrene ($(C_8H_8)_n$) and 2 μm Kapton ($C_{22}H_{10}N_2O_5$), each deposited on Al_2O_3 substrates by spin-coating. The bottom electrode/ferroelectric capacitor stack was fabricated on these polymer surfaces at room temperature. Figure 8(a) shows x-ray diffraction θ–2θ scans for both sample types. Despite the low-temperature growth, Pt was predominantly ⟨111⟩ oriented while $Zn_{1-x}Mg_xO$ films were uniformly ⟨0001⟩. In both cases, small populations of (200)- and (311)-oriented Pt were present, about ten times more prevalent on the polystyrene surface.

The 0002 rocking curves for $Zn_{1-x}Mg_xO$ on polystyrene and Kapton are 8.7° and 4.8°, respectively; stronger mosaicity in the case of polystyrene likely originates from the less-well textured Pt. The ferroelectric response for both samples is shown in Fig. 8(b). Both capacitors show clear polarization reversal with coercive voltages of ∼3 MV cm^{-1}, but P_r values are ∼25 and ∼100 μC cm^{-2} on polystyrene and Kapton, respectively; the difference is likely linked to mosaic spread. While the results are preliminary, this demonstrates unambiguously the ability to integrate $Zn_{1-x}Mg_xO$ directly onto polymeric surfaces and substrates.

CONCLUSIONS

Robust ferroelectricity is demonstrated in highly insulating Mg-substituted ZnO thin films. Polarization is field-reversible for Mg concentrations between ∼30% and ∼37%. Below this range, breakdown occurs before switching, and above this range the films phase separate. Remanent polarization values can exceed 100 μC/cm^2, with low-field dielectric loss tangents below 1% and low-field permittivities approaching 14 in the ferroelectric window. Ferroelectric ZnMgO films exhibit a pronounced wake-up process during which polarization evolves over a period of ∼100 field cycles at a maximum field just greater than the coercive field. Finally, ferroelectric $Zn_{1-x}Mg_xO$ thin film stacks with Pt electrodes can be prepared without intentional substrate heating, i.e., energy during deposition originates exclusively from the plasma with electrical properties identical to those prepared at 200 °C. This near-ambient-temperature deposition enables direct integration of

$Zn_{1-x}Mg_xO$ ferroelectric capacitors on polymer substrates including Kapton and polystyrene as demonstrated presently.

SUPPLEMENTARY MATERIAL

See the supplementary material for the complete structural, optical, and electrical analysis of the studied $Zn_{1-x}Mg_xO$ thin films.

ACKNOWLEDGMENTS

This research was primarily supported as part of the Center for 3D Ferroelectric Microelectronics (3DFeM), an Energy Frontier Research Center funded by the U.S. Department of Energy (DOE), Office of Science, Basic Energy Sciences under Award No. DE-SC0021118. Activities supported include all film growth, all film physical characterization (besides TEM), all electrical property measurements that are included in this manuscript, and the majority of data analysis and interpretation. The Army Research Office (ARO) and the Defense Advanced Research Projects Agency (DARPA) via Project No. W911NF-20-2-0274 supported the role of J.H. who contributed to the design of the experiments and to the data analysis and interpretation. The National Science Foundation (NSF), as part of the Center for Dielectrics and Piezoelectrics under Grant Nos. IIP-1841453 and IIP-1841466, supported preliminary experiments on ZnO–MgO preparation, upon which the present findings are based on. S.B. and N.A. acknowledge NSF CAREER (No. DMR-1654107), which supported 50% of the TEM analysis. This work utilized resources provided by the NSF-MRSEC-sponsored Materials Characterization Lab at Penn State.

DATA AVAILABILITY

The data that support the findings of this study are available within the article and its supplementary material.

REFERENCES

[1]Z. Fan, J. Chen, and J. Wang, "Ferroelectric HfO_2-based materials for next-generation ferroelectric memories," J. Adv. Dielectr. **6**, 1630003 (2016).
[2]K. Florent *et al.*, "Understanding ferroelectric Al:HfO_2 thin films with Si-based electrodes for 3D applications," J. Appl. Phys. **121**, 204103 (2017).
[3]J. F. Scott, L. D. McMillan, and C. A. Araujo, "Switching kinetics of lead zirconate titanate sub-micron thin-film memories," Ferroelectrics **93**, 31–36 (1989).
[4]T. P. Ma and J. P. Han, "Why is nonvolatile ferroelectric memory field-effect transistor still elusive?," IEEE Electron Device Lett. **23**, 386–388 (2002).
[5]H. Kohlstedt *et al.*, "Current status and challenges of ferroelectric memory devices," Microelectron. Eng. **80**, 296–304 (2005).
[6]Y. S. Kim *et al.*, "Critical thickness of ultrathin ferroelectric $BaTiO_3$ films," Appl. Phys. Lett. **86**, 102907 (2005).
[7]V. Nagarajan *et al.*, "Misfit dislocations in nanoscale ferroelectric heterostructures," Appl. Phys. Lett. **86**, 192910 (2005).
[8]J. F. Ihlefeld *et al.*, "Scaling effects in perovskite ferroelectrics: Fundamental limits and process-structure-property relations," J. Am. Ceram. Soc. **99**, 2537–2557 (2016).
[9]A. von Hippel, "Piezoelectricity, ferroelectricity, and crystal structure," Z. Phys. **133**, 158–173 (1952).
[10]H. Megaw, *Ferroelectricity in Crystals* (Metheun & Co., 1957).
[11]G. Burns, *Solid State Physics* (Academic Press, 1985).
[12]J. Müller *et al.*, "Ferroelectricity in yttrium-doped hafnium oxide," J. Appl. Phys. **110**, 114113 (2011).
[13]S. Fichtner, N. Wolff, F. Lofink, L. Kienle, and B. Wagner, "AlScN: A III-V semiconductor based ferroelectric," J. Appl. Phys. **125**, 114103 (2019).
[14]J. Hayden *et al.*, "Ferroelectricity in boron-substituted aluminum nitride thin films," Phys. Rev. Mater. **5**, 044412 (2021).
[15]R. F. Cava, W. F. Peck, and J. J. Krajewski, "Enhancement of the dielectric constant of Ta_2O_5 through substitution with TiO_2," Nature **377**, 215–217 (1995).
[16]G. L. Brennecka and D. A. Payne, "Preparation of dense Ta_2O_5-based ceramics by a coated powder method for enhanced dielectric properties," J. Am. Ceram. Soc. **89**, 2089–2095 (2006).
[17]H. Moriwake *et al.*, "Ferroelectricity in wurtzite structure simple chalcogenide," Appl. Phys. Lett. **104**, 242909 (2014).
[18]K. Koike *et al.*, "Molecular beam epitaxial growth of wide bandgap ZnMgO alloy films on (1 1 1)-oriented Si substrate toward UV-detector applications," J. Cryst. Growth **278**, 288–292 (2005).
[19]X. Kang *et al.*, "Enhanced dielectric and piezoelectric responses in $Zn_{1-x}Mg_xO$ thin films near the phase separation boundary," Appl. Phys. Lett. **110**, 042903 (2017).
[20]P. Kumar, H. K. Malik, A. Ghosh, R. Thangavel, and K. Asokan, "Bandgap tuning in highly c-axis oriented $Zn_{1-x}Mg_xO$ thin films," Appl. Phys. Lett. **102**, 221903 (2013).
[21]T. Minemoto, T. Negami, S. Nishiwaki, H. Takakura, and Y. Hamakawa, "Preparation of $Zn_{1-x}Mg_xO$ films by radio frequency magnetron sputtering," Thin Solid Films **372**, 173–176 (2000).
[22]A. Ohtomo *et al.*, "$Mg_xZn_{1-x}O$ as a II-VI widegap semiconductor alloy," Appl. Phys. Lett. **72**, 2466 (1998).
[23]A. Onodera, N. Tamaki, Y. Kawamura, T. Sawada, and H. Yamashita, "Dielectric activity and ferroelectricity in piezoelectric semiconductor Li-doped ZnO," Jpn. J. Appl. Phys. **35**, 5160–5162 (1996).
[24]A. Onodera, N. Tamaki, K. Jin, and H. Yamashita, "Ferroelectric properties in piezoelectric semiconductor $Zn_{1-x}M_xO$ (M = Li, Mg)," Jpn. J. Appl. Phys. **36**, 6008 (1997).
[25]Y.-H. Lin, M. Ying, M. Li, X. Wang, and C.-W. Nan, "Room-temperature ferromagnetic and ferroelectric behavior in polycrystalline ZnO-based thin films," Appl. Phys. Lett. **90**, 222110(2007).
[26]M. Joseph, H. Tabata, and T. Kawai, "Ferroelectric behavior of Li-doped ZnO thin films on Si(100) by pulsed laser deposition," Appl. Phys. Lett. **74**, 2534–2536 (1999).
[27]A. Onodera and M. Takesada, "Ferroelectricity in simple binary crystals," Crystals **7**, 232 (2017).
[28]N. W. Emanetoglu *et al.*, "$Mg_xZn_{1-x}O$: A new piezoelectric material," IEEE Trans. Ultrason. Ferroelectr. Freq. Control **50**, 537–543 (2003).
[29]T. Minemoto *et al.*, "Preparation of $Zn_{1-x}Mg_xO$ films by radio frequency magnetron sputtering," Thin Solid Films **372**, 173–176 (2000).
[30]M. Rouchdi, E. Salmani, B. Fares, N. Hassanain, and A. Mzerd, "Synthesis and characteristics of Mg doped ZnO thin films: Experimental and ab-initio study," Results Phys. **7**, 620–627 (2017).
[31]H. Hayashi *et al.*, "$Zn_{1-x}Mg_xO$ second buffer layer of $Cu_2Sn_{1-x}Ge_xS_3$ thin-film solar cell for minimizing carrier recombination and open-circuit voltage deficit," Sol. Energy **204**, 769–776 (2020).
[32]O. Gencyilmaz, F. Atay, and I. Akyuz, "Fabrication and characterization of $Zn_{1-x}Mg_xO$ films for photovoltaic application," in *Progress in Clean Energy* (Springer, Cham, 2015), Vol. 1, pp. 1–968.
[33]M. Akiyama *et al.*, "Enhancement of piezoelectric response in scandium aluminum nitride alloy thin films prepared by dual reactive cosputtering," Adv. Mater. **21**, 593–596 (2009).
[34]M. Akiyama, T. Kamohara, K. Kano, A. Teshigahara, and N. Kawahara, "Influence of oxygen concentration in sputtering gas on piezoelectric response of aluminum nitride thin films," Appl. Phys. Lett. **93**, 021903 (2008).
[35]S.-H. Jang and S. F. Chichibu, "Structural, elastic, and polarization parameters and band structures of wurtzite ZnO and MgO," J. Appl. Phys. **112**, 073503 (2012).

[36]S. Gowrishankar, L. Balakrishnan, and N. Gopalakrishnan, "Band gap engineering in $Zn_{(1-x)}Cd_xO$ and $Zn_{(1-x)}Mg_xO$ thin films by RF sputtering," Ceram. Int. **40**, 2135–2142 (2014).
[37]I. S. Kim and B. T. Lee, "Structural and optical properties of single-crystal ZnMgO thin films grown on sapphire and ZnO substrates by RF magnetron sputtering," J. Cryst. Growth **311**, 3618–3621 (2009).
[38]M. M. Fan *et al.*, "Realization of cubic ZnMgO photodetectors for UVB applications," J. Mater. Chem. C **3**, 313–317 (2015).
[39]J.-L. Yang, K.-W. Liu, and D.-Z. Shen, "Recent progress of ZnMgO ultraviolet photodetector," Chin. Phys. B **26**, 047308 (2017).
[40]R. Ondo-Ndong, H. Essone-Obame, Z. H. Moussambi, and N. Koumba, "Capacitive properties of zinc oxide thin films by radiofrequency magnetron sputtering," J. Theor. Appl. Phys. **12**, 309–317 (2018).
[41]J. S. Thorp, N. E. Rad, D. Evans, and C. D. H. Williams, "The temperature dependence of permittivity in MgO and Fe-MgO single crystals," J. Mater. Sci. **21**, 3091–3096 (1986).
[42]H. Ono, M. Nakahata, F. Tsukihashi, and N. Sano, "Determination of standard Gibbs energies of formation of MgO, SrO, and BaO," Metall. Trans. B **24**, 487–492 (1993).
[43]Y. Li and X. Wu, "The standard molar enthalpies of formation of nano-ZnO particles with different morphologies," J. Nanomater. **2015**, 738909.
[44]J. Lettieri, J. H. Haeni, and D. G. Schlom, "Critical issues in the heteroepitaxial growth of alkaline-earth oxides on silicon," J. Vac. Sci. Technol. A **20**, 1332–1340 (2002).
[45]S. Okamura, M. Takaoka, T. Nishida, and T. Shiosaki, "Increase in switching charge of ferroelectric $SrBi_2Ta_2O_9$ thin films with polarization reversal," Jpn. J. Appl. Phys. **39**, 5481–5484 (2000).
[46]D. Zhou *et al.*, "Wake-up effects in Si-doped hafnium oxide ferroelectric thin films," Appl. Phys. Lett. **103**, 192904 (2015).
[47]M. Andritschky, F. Guimarães, and V. Teixeira, "Energy deposition and substrate heating during magnetron sputtering," Vacuum **44**, 809–813 (1993).
[48]R. H. Reuss *et al.*, "Macroelectronics: Perspectives on technology and applications," Proc. IEEE **93**, 1239–1256 (2005).
[49]V. Lumelsky, M. Shur, S. Wagner, and M. Ding, "Special issue on sensitive skin," Int. J. High Speed Electron. Syst. **10**, 413 (2000).
[50]S. R. Forrest, "Electronic appliances on plastic," Nature **428**, 911–918 (2004).
[51]J. Rho, S. Kim, N. E. Lee, H. S. Lee, and J. H. Ahn, "$PbZr_xTi_{1-x}O_3$ ferroelectric thin-film capacitors for flexible nonvolatile memory applications," IEEE Electron Device Lett. **31**, 1017–1019 (2010).
[52]R. D. Shannon, and C. T. Prewitt, "Effective ionic radii in oxides and fluorides," Acta Cryst. B **25**, 925–946 (1969).